Nanoscale

ROYAL SOCIETY OF CHEMISTRY

PAPER

View Article Online
View Journal | View Issue



Cite this: *Nanoscale*, 2025, **17**, 13229

# Nanophotonics of mid-infrared plasmon-polaritons at interfaces between metals and two-dimensional crystals†

Flávio H. Feres, *[a] Ingrid D. Barcelos, [a] Dario A. Bahamon,[b,c] João E. Levandoski, [d] Andrea Mancini, [e] Thiago M. dos Santos, [a] Rafael A. Mayer, [a,f] Davi H. S. Camargo,[g] Carlos C. B. Bufon,[h] Adrian Cernescu,[i] Stefan A. Maier, [j,k] Raul de O. Freitas [a] and Francisco C. B. Maia *[a]

The optical response of metal/dielectric interfaces is largely influenced by surface plasmon-polariton (SPP) modes. In the mid-infrared (IR) range, SPPs can probe the inner physicochemical properties of metal/dielectric systems, including interfaces with mid-IR polaritonic 2D crystals. Using advanced nanoscopy techniques, we characterize mid-IR SPP modes at air/gold and hexagonal boron nitride (hBN) 2D crystal/gold interfaces *via* synchrotron infrared nanospectroscopy (SINS) and scattering-scanning near-field optical microscopy (s-SNOM) imaging. SPPs in these systems show micrometer-sized wavelengths and propagation lengths over 20 micrometers at room temperature. In hBN/Au, both SPPs and hyperbolic phonon polaritons (HPhPs) coexist, creating SPP–HPhP wave superposition. The experimental momentum and damping of the SPP waves are determined from the s-SNOM imaging and the SINS spatio-spectral linescan. Thereby, we retrieve the experimental frequency–momentum dispersion relation, presenting excellent agreement with theory. Furthermore, we characterize an anti-crossing of the SPP dispersion near the in-plane transverse optical phonon frequency of hBN, indicating that SPP modes and phonon form a coupled system interacting in the strong coupling regime. Such an interaction of SPPs with phonons can be further explored to enhance the sensibility of mid-IR nanospectroscopy techniques.

Received 31st October 2024,
Accepted 23rd April 2025

DOI: 10.1039/d4nr04543b

rsc.li/nanoscale



Surface plasmon-polaritons (SPP),[1,2] quasi-particles originating from the coupling of photons to collective oscillations of free charge carriers, are intrinsically two-dimensional (2D) modes confined to the interface between a material of metallic character and a dielectric one. Such ultimate 2D confinement originates from the fact that while SPPs are propagative modes in the interface plane, they are evanescent along the interface normal direction. Being genuinely photon-charge coupled modes intrinsic to the optical near-field electromagnetic zone, SPP waves possess intertwined optical and electronic properties, leading to their exploitation from the ultraviolet-visible to near-infrared (IR) ranges in waveguiding,[3] plasmonic circuits,[3,4] sensing,[5] lasing,[6–8] light harvesting[5] and for quantum information processing.[9] In the mid-IR, SPPs have been studied in metallic structures engineered to achieve high confinement of electromagnetic modes as IR nanofocusing in tapered transmission line waveguides.[10–12] Moreover, mid-IR SPPs are found as stationary and localized modes in antennas[10,13–15] and resonators[16,17] of semiconducting[18] and metallic[19] micro- and nanostructures. Furthermore, mid-IR SPPs are theoretically predicted to allow for accessing and retrieving invaluable information from physicochemical properties of general dielectric/metal (D/M) interfaces associated with molecular vibrations, electronic transitions, and room temperature thermodynamical reactions.[17] In the pursuit of such great conceptual potential, we present here a thorough

[a]*Brazilian Synchrotron Light Laboratory (LNLS), Brazilian Center for Research in Energy and Materials (CNPEM), Zip Code 13083-970 Campinas, Sao Paulo, Brazil. E-mail: flavio.feres@lnls, francisco.maia@lnls.br*
[b]*MackGraphe – Graphene and Nanomaterials Research Institute, Mackenzie Presbyterian University, São Paulo – 01302-907, Brazil*
[c]*School of Engineering, Mackenzie Presbyterian University, São Paulo – 01302-907, Brazil*
[d]*Department of Materials and Bioprocesses Engineering, School of Chemical Engineering, University of Campinas, Campinas, Brazil*
[e]*Chair in Hybrid Nanosystems, Nanoinstitute Munich, Ludwig-Maximilians-Universität Munich, Königinstrasse 10, 80539 Munich, Germany*
[f]*Physics Department, Gleb Wataghin Physics Institute, University of Campinas (Unicamp), 13083-859 Campinas, Sao Paulo, Brazil*
[g]*Brazilian Laboratory of Nanotechnology (LNNano), Brazilian Center for Research in Energy and Materials (CNPEM), Zip Code 13083-970 Campinas, Sao Paulo, Brazil*
[h]*Institute of Geosciences and Exact Sciences, São Paulo State University (UNESP), Rio Claro, Brazil*
[i]*Attocube Systems AG, 85540 Haar-Munich, Germany*
[j]*School of Physics and Astronomy, Monash University, Clayton, 3800 VIC, Australia*
[k]*Blackett Laboratory, Imperial College London, London, SW7 2AZ, UK*
† Electronic supplementary information (ESI) available. See DOI: https://doi.org/10.1039/d4nr04543b

characterization of mid-IR SPP waves at D/M interfaces, using scattering-type scanning near-field optical microscopy (s-SNOM)[20] and synchrotron infrared nanospectroscopy (SINS).[21] Our study not only reveals fundamental nanophotonic properties of SPPs but also demonstrates that these waves can deeply probe matter through strong coupling (SC) with phonons. SC phenomena in nanophotonics have garnered significant attention due to their potential to reach and manipulate new hybrid quantum states[22] as recently shown from SC interaction between polaritons of van der Waals (vdW) crystals and vibrational modes of organic molecules.[23] Additionally, new polaritonic modes arising from SC between hyperbolic phonon polaritons (HPhPs) in hetero-bicrystals have been observed, enabling exquisite optical phenomena such as negative refraction and negative group velocity.[24,25] Interactions between SPPs and phonons have also been documented in graphene hexagonal boron nitride (hBN)[26,27] and carbon nanotubes–hBN[28] heterostructures. Here we aim to expand the understanding of SC phenomena in 2D systems by reporting, for the first time, the SC regime between long-range SPPs on gold (Au) and optical phonons in hyperbolic crystals.

In this work a full characterization of SPPs at mid-IR frequencies is achieved by investigating the D/M interfaces: (i) Au/$SiO_2$, a 90 nm thick film of Au sputtered onto a 2 μm-thick layer of $SiO_2$ and (ii) hBN/Au, a hBN 2D crystal deposited onto Au surface (see the Experimental Methods section for details on techniques and sample construction). The s-SNOM images and SINS spectral linescans provide a complete data set permitting us to quantify the complex momentum $q_{SPP}$, where $q_{SPP} = q_{SPP} + i\gamma_{SPP}$, ($mq_{SPP}$ is the propagative momentum part and $\gamma_{SPP}$ is the damping) for each excitation frequency ($\omega$). This analysis produces the experimental frequency–momentum dispersion relation, $\omega$–$q_{SPP}$, governing the SPP waves. Moreover, s-SNOM and SINS nanoimagings also reveal the superposition of SPP and HPhP waves of hBN. The phenomenon is observed for different $\omega$ values in the hBN upper Reststhralen (RS) band, which is defined as that in between the transversal (TO), $\omega_{TO}$ = 1365 $cm^{-1}$, and the longitudinal optical (LO) phonons, $\omega_{LO}$ = 1610 $cm^{-1}$.[29–32] The wave superposition results from the interference between high momenta HPhPs ($q_{HPhP} \sim 10^5$ $cm^{-1}$)[14,29–32] and low momenta SPPs ($q_{SPP} \sim 10^4$ $cm^{-1}$). We remark that HPhP modes in metallic substrates have been referred to as hyperbolic image polaritons (HIP)[33,34] formed due to the coupling of the mode in the polaritonic medium with its image in the metal. As observed, the HIPs present larger confinement (higher momentum) than the analogues formed when the polaritonic medium lies on dielectric substrates.[30]

To understand these polariton modes, we compute the theoretical dispersion by solving the Maxwell equations at the D/M interface.[35] The calculations yield a parameter-free $\omega$–$q_{SPP}$ dispersion in good quantitative agreement with the experimental observations. Moreover, both theoretical and experimental dispersions feature an anti-crossing (AC) effect near the hBN $\omega_{TO}$. Our analysis demonstrates that the AC arises from the interaction of SPP waves with the hBN phonon in the SC regime as evaluated from a coupled oscillator model.[23,28]

The s-SNOM and SINS experimental schemes and the hBN (60 nm)/Au (90 nm)/$SiO_2$ (2 μm) sample architecture are sketched in Fig. 1a (see the Experimental Methods for details). The scheme also features the SPP–HPhP wave superposition representing the main polariton modes herein discussed. Fig. 1b presents the AFM topography of the sample that, concisely, was constructed by transferring the hBN crystal onto the Au film which was deposited by an electron beam onto the $SiO_2$/Si surface. Part of the hBN flake is suspended over a 2.5 μm-width groove made by lithography in the Au film. An Au disk-like antenna resides atop the hBN crystal. In Fig. 1c and d, we present s-SNOM images of the third harmonic amplitude ($S_3$) signal using a quantum cascade laser (QCL) as the excitation source. These measurements were performed by tuning the QCL at $\omega$ = 1470 $cm^{-1}$, which is inside the upper RS band of hBN, and at $\omega$ = 1200 $cm^{-1}$, which is outside any hBN RS band. They reveal distinguishable optical patterns on hBN/Au/$SiO_2$ and Au/$SiO_2$, stemming from HPhP and SPP waves of different wavelengths, which are discussed in detail in Fig. 2.

As seen in Fig. 2a, polaritonic patterns are produced by the interference between SPP and HPhP waves launched both by the disk-like antenna and by the groove edge. The corresponding polaritonic profiles are plotted in Fig. 2b. The profile $P'_1$ permits good visualization of the SPP–HPhP superposition: the SPP wave of lower momentum ($q_{SPP}$) interfering with the HPhP wave of higher momentum ($q_{HPhP}$). All scans were performed orthogonally to the groove, ensuring consistency with the conditions described in ref. 36–40. Further details on data extraction and SPP momenta calculations, based on the illumination geometry, are discussed in the ESI.† To obtain quantitative information, we model the resultant polaritonic field ($E$) as a superposition of SPP ($E^e_{SPP}$) and HPhP ($E^e_{HPhP}$) waves in the form of damped plane waves:

$$E = E^e_{HPhP} + E^e_{SPP} + C = A_{HPhP}e^{-i(q_{HPhP}-i\gamma_{HPhP})x-i\theta} + A_{SPP}e^{-i(q_{SPP}-i\gamma_{SPP})x} + C \quad (1)$$

This equation consists of the summation over HPhP and SPP complex fields and a complex non-propagative background $C$. In the analytical form, each damped plane wave is defined by the parameters: amplitude $A_\alpha$, momentum $q_\alpha$ and

**Francisco C. B. Maia**

*Francisco C. B. Maia is a researcher at the infrared beamline Imbuia of Sirius, the Brazilian Synchrotron (LNLS/CNPEM). Over the last 10 years, he has dedicated efforts toward research in the great area of near-field nano-optics and the nanophotonics of two-dimensional materials.*

 

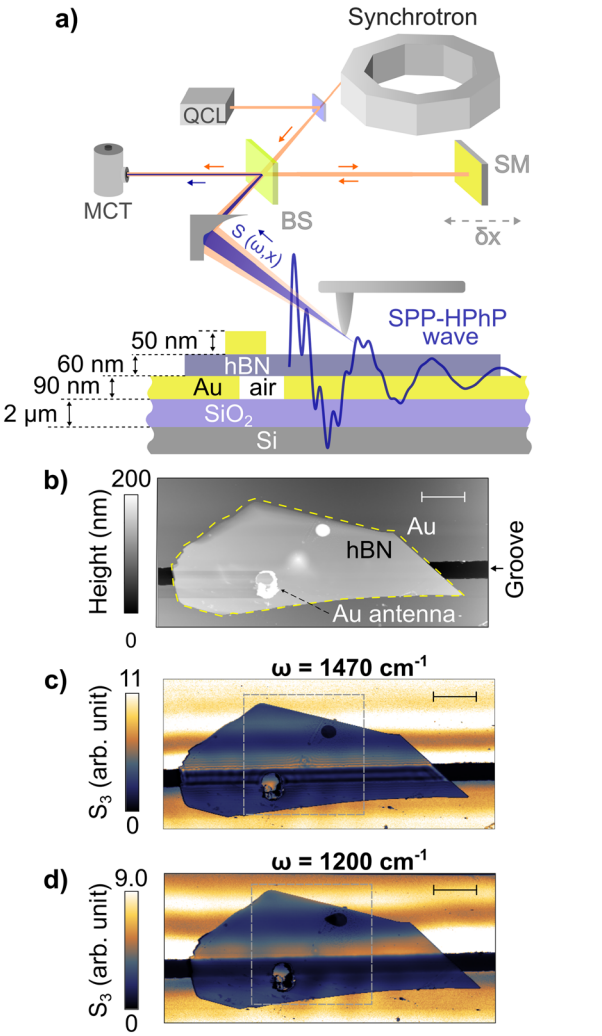


**Fig. 1** s-SNOM and SINS schematics and interferometric measurements of polariton modes. (a) s-SNOM and SINS experimental schemes probing a SPP–HPhP wave in hBN/Au/$SiO_2$. Both techniques use an asymmetric Michelson interferometer, formed by a beamsplitter (BS) and a scanning mirror (SM), and a mercury-cadmium-telluride (MCT) detector (further details in the Experimental Methods section). The thicknesses of each material layer are given. (b) Sample topography. (c) and (d) s-SNOM third harmonic amplitude ($S_3$) images at $\omega$ = 1470 $cm^{-1}$ and $\omega$ = 1200 $cm^{-1}$, respectively. The gray squares in (c) and (d) indicate regions examined in Fig. 2. Scale bars: 5 μm.

damping $\gamma_\alpha$, with $\alpha$ = SPP or HPhP. For generalization, a relative phase difference $\theta$ between the SPP and HPhP waves is considered. These parameters are determined by fitting eqn (1) to experimental profiles. It is noteworthy that our model includes only edge- and antenna-launched waves. In our data, there is no experimental evidence of tip-launched waves that would introduce half-wavelength contributions from reflected polariton waves at crystal edges.[29,31,41,42]

The model fit to the profile $P'_1$ (Fig. 2b) yields $q_{SPP}$ = 1.12 × $10^4$ $cm^{-1}$ and $q_{HPhP}$ = 18.8 × $10^4$ $cm^{-1}$. Since the wavelength $\lambda = 2\pi/q$, it is verified that $\lambda_{SPP} > \lambda_{HPhP}$ in $P'_1$ as stated above. For the profile $P'_2$, extracted from the hBN region onto the groove (Fig. 2a), we determine $q_{HPhP}$ = 6.14 × $10^4$ $cm^{-1}$ and $q_{SPP}$ = 1.57 × $10^4$ $cm^{-1}$. It is important to comment that the SPP wave in this profile is created propagate in the groove orthogonal edges, forming an SPP slit waveguide.[43] Moreover, in agreement with the literature on HPhP modes of the upper RS band of hBN lying on metallic and dielectric substrates,[30,31,33,34,41,44] our analysis finds a larger value of $q_{HPhP}$ on Au in the $P'_1$ than that in air in the $P'_2$. To estimate the accuracy of our approach, we calculate the expected $q_{HPhP}$ values using the Fresnel coefficients for p-polarized modes.[32] The theoretically predicted momentum values for HPhP are 19.6 × $10^4$ $cm^{-1}$ on Au and 7 × $10^4$ $cm^{-1}$ in air. Such calculations are reasonably close to the model-determined ones from the $P'_1$ and $P'_2$ experimental profiles, respectively: 18.8 × $10^4$ $cm^{-1}$ on Au and 6.14 × $10^4$ $cm^{-1}$ in air. To complement this discussion, we plot in Fig. 2c the $S_3$ image at $\omega$ = 1470 $cm^{-1}$ of edge-launched SPP waves in Au/$SiO_2$ without hBN. The model-fit to the profile $P'_3$ (Fig. 2d) yields $q_{SPP}$ = 1.35 × $10^4$ $cm^{-1}$. In the ESI,† Fourier analyses of these investigated profiles clearly distinguish the SPP and HPhP momenta components, thus, corroborating our modelling results.

To compare, Fig. 2e and h present $S_3$ images of the sample illuminated at $\omega$ = 1200 $cm^{-1}$ where no HPhPs are excited in hBN as the frequency lies outside the upper RS band. Hence, only SPP waves are visualized in the profiles $P_1$ and $P_2$ (Fig. 2f). To fit these profiles, the eqn (1) model is used with one propagative term ascribed to the SPP wave, as confirmed by Fourier transform analysis (ESI†). In Fig. 2g, we observe edge-launched SPP waves in Au/$SiO_2$, with $q_{SPP}$ = 1.14 × $10^4$ $cm^{-1}$ as determined from the model-fit to $P_3$ (Fig. 2h).

To further our analyses, we inspect the SPP waves in a broader range by a spatio-spectral linescan from SINS technique (Fig. 1a). This measurement consists of a distance × $\omega$ map built by plotting a set of SINS spectra acquired along a defined trajectory.[45] In Fig. 3a, we present the spatio-spectral linescan of the second harmonic amplitude, $S_2(\omega, x)$, signal on hBN/Au normalized by the SINS spectrum on a clean Au surface. For better visualization of different polaritons fringes, we re-normalized the measurement by the spectrum at $x$ = 20 μm, which removes signal saturation due to the high reflectivity at the $\omega_{TO}$ phonon resonance. The scanned path begins at the groove edge and extends up to $x$ = 20 μm on the 2D crystal as denoted in Fig. 1a. It is displayed the 1320–1420 $cm^{-1}$ range, including part of the hBN upper RS band (above 1365 $cm^{-1}$). One can see the fringes of high-momentum HPhP modes (indicated by the white arrow in Fig. 3a) propagating from the groove edge up to $x \approx 3$ μm. The SPP modes rise (blue arrows in Fig. 3a) across the entire spectral range, emphasizing their broadband character, and reach $x$ = 20 μm. Intriguingly, near the hBN $\omega_{TO}$ = 1365 $cm^{-1}$, we note a spatio-spectral variation of the SPP modes. The correlation of such distortion with the $\omega_{TO}$ is noted from the correspondence with the phonon resonance of the in-plane hBN permittivity $\varepsilon_{\perp}^{hBN}$ plotted on the right panel of Fig. 3a. Moreover, the feature is not found in the Au/$SiO_2$ linescan for the same spectral range (see the ESI†). To retrieve quantitative information from this phenomenon, we analyzed SPP profiles extracted near the phonon peak at $\omega$ = 1408 $cm^{-1}$, 1363 $cm^{-1}$, and 1326 $cm^{-1}$ (Fig. 3b). Eqn (1) fittings to these data reveal that the 1363 $cm^{-1}$ profile, which is closer to

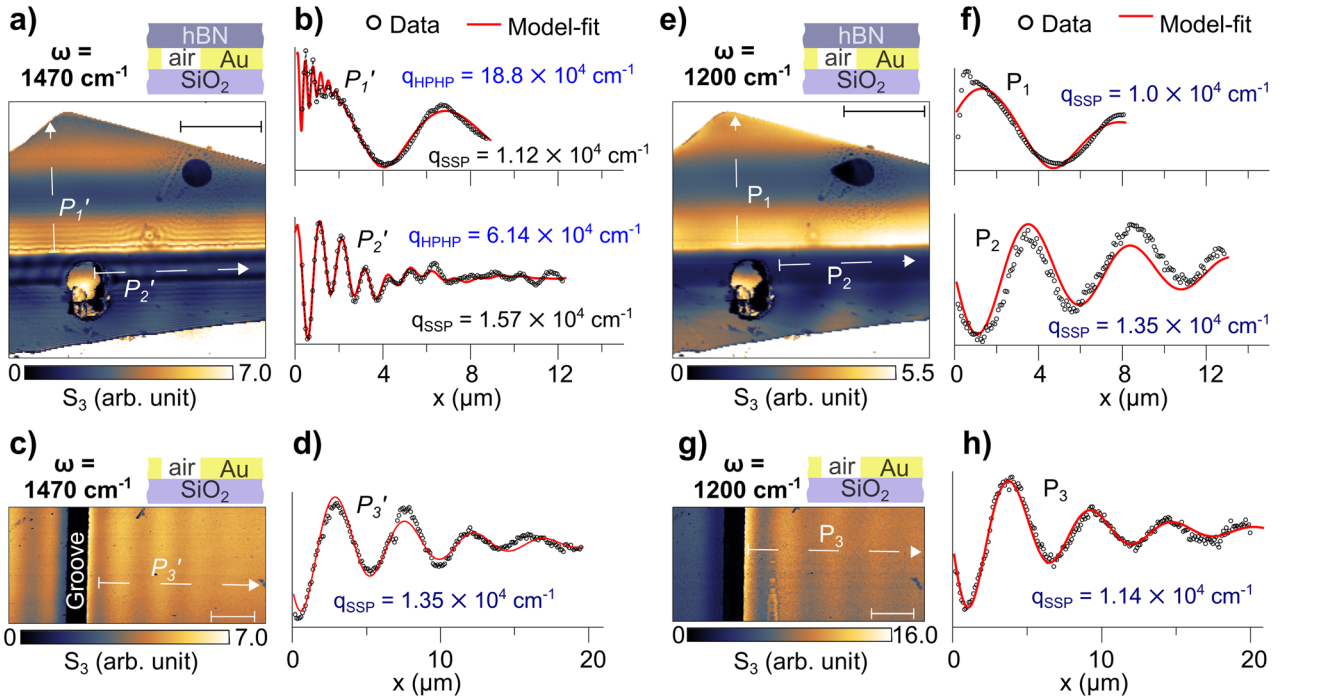


**Fig. 2** Imaging of SPP and HPhP waves. (a) $S_3$ image at $\omega$ = 1470 cm$^{-1}$ from the area indicated in Fig. 1c (gray square). (b) $P_1'$ and $P_2'$ polariton profiles, extracted from locations shown in (a), with the corresponding model-fits (red curves) and the obtained $q_{SPP}$ and $q_{HPhP}$. (c) $S_3$ image at $\omega$ = 1470 cm$^{-1}$ of the Au/$SiO_2$ interface and (d) the polariton profile $P_3'$, extracted from (c) with the corresponding model-fit (red curve) and $q_{SPP}$ value. (e–h) Comparative images for excitation at $\omega$ = 1200 cm$^{-1}$. Scale bars: 5 μm.

$\omega_{TO}$, possesses larger damping, $\gamma_{SPP}$ = 0.41 × 10$^4$ cm$^{-1}$, than that of the other frequencies. This is a characteristic behavior of anti-crossing (AC) effect that can be ascribed to the phonon–SPP interaction. In analogy to the reported HPhPs coupled to molecular modes, the phonon–SPP interaction leads to significant modification of $q_{SPP}$ and a considerable increase in $\gamma_{SPP}$.[23]

To elucidate such effect, we compute the SPP experimental $\omega$–$q$ dispersion, from the linescan data, employing the expression

$$\mathrm{Re}[\tilde{s}(q,\omega)] = \frac{1}{\sqrt{2\pi}}\left[\frac{q_{SPP}(\omega)}{(q_{SPP}-q)^2+\gamma_{SPP}{}^2(\omega)}\right], \quad (2)$$

which is the real part of the Fourier transform of a damped plane wave. This equation allows obtaining the experimental dispersion relation by using as inputs the $q_{SPP}$ and $\gamma_{SPP}$ values acquired from fitting the SPP profiles from Fig. 3a data to eqn (1) (see ESI section III for details†). To accurately determine the values of $q_{SPP}$, we analyzed the extracted in-plane momentum from the profiles, which arises from the interference between the incident illumination ($k_0 \sin\theta$, where $\theta$ is the angle between the illumination and the tip) and $q_{SPP}$ (see the ESI†). Our analyses are in concordance with previous studies[36–40] considering $\theta = \pi/3$, where the measured period of the fringes ($\lambda_{eff}$) is given by $\lambda_{eff} = \dfrac{\lambda_{SPP}}{1-(\lambda_{SPP}/\lambda_0)\sin\theta}$.

Considering this correction, the experimental $\omega$–$q$ dispersion of SPP modes is plotted in Fig. 4a.

To compare the experimental dispersion with theory, we calculate the theoretical $q_{SPP}$ and $\gamma_{SPP}$ for hBN/Au from.

$$q_{SPP}(\omega) + i\gamma_{SPP}(\omega) = k_0\sqrt{\frac{\left(\varepsilon_{\parallel}^{hBN}\varepsilon_{Au}\right)\left(\varepsilon_{\perp}^{hBN}-\varepsilon_{Au}\right)}{\varepsilon_{\parallel}^{hBN}\varepsilon_{\perp}^{hBN}-\varepsilon_{Au}{}^2}} \quad (3)$$

In the absence of external sources, eqn (3) is derived from Maxwell's equations in the D/M system (considering both media as being semi-infinite) accounting for the boundary conditions at all interfaces.[35] The terms $\varepsilon_{\perp}^{hBN}$ and $\varepsilon_{\parallel}^{hBN}$ are the in- and out-of-plane components of the hBN electrical permittivity tensor, $\varepsilon_{Au}$ is the Au permittivity and $k_0$ is the momentum of light in free space. Hence, we use the theoretical $q_{SPP}$ and $\gamma_{SPP}$ from eqn (3) as inputs to eqn (2) to plot the theoretical dispersion shown in Fig. 4b.

Comparing Fig. 4a and b we note that experiment and theory quantitatively agree regarding momenta and damping values. The AC effect also consistently appears around $\omega_{TO}$ in both analyses.

A further evaluation of the SPP–phonon interaction, cause of the AC effect, is given by the classical model of coupled harmonic oscillators.[23,28,46] This model can be described by the pair of coupled equations of motion

$$\begin{cases} \ddot{x}_{SPP}(t) + \Gamma_{SPP}\dot{x}_{SP}(t) + \omega_{SPP}{}^2 x_{SPP}(t) - \Omega\bar{\omega}x_P(t) = F_{SPP}(t) \\ \ddot{x}_P(t) + \Gamma_P\dot{x}_{PP}(t) + \omega_P{}^2 x_P(t) - \Omega\bar{\omega}x_{SPP}(t) = F_P(t) \end{cases}, \quad (4)$$

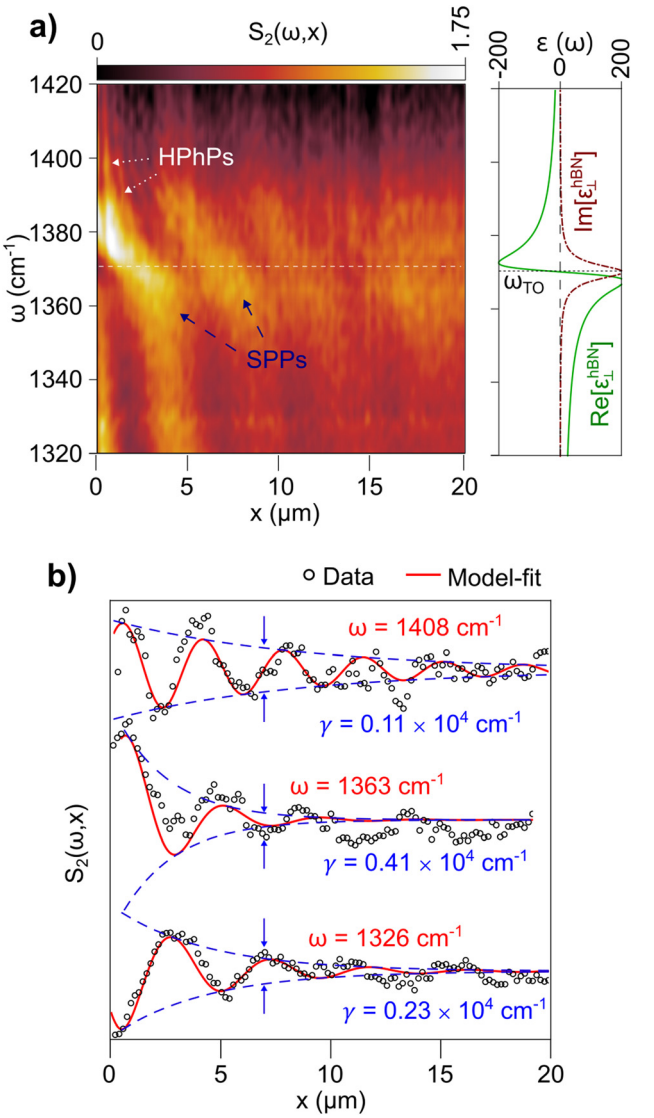


**Fig. 3** Anti-crossing near the in-plane hBN phonon visualized by the SINS line scan. (a) $S_2$ linescan on hBN across the groove edge. The hBN in-plane permittivity – real ($\mathrm{Re}[\varepsilon_{\perp}^{BN}]$) and imaginary ($\mathrm{Im}[\varepsilon_{\perp}^{hBN}]$) – component featuring the resonance at $\omega_{TO}$ = 1365 $cm^{-1}$ (right-hand panel). (b) Profiles extracted along the *x*-axis with the respective model-fits.

where the parameters ($\omega_{SPP}$, $\omega_P$), ($\Gamma_{SPP}$, $\Gamma_P$) and ($x_{SPP}$, $x_P$) are the resonant frequencies, dampings and displacements of the coupled SPP and phonon (P) modes, respectively. $F_{SPP}$ and $F_P$ are the effective driving forces, proportional to the excitation electric field, acting on the two modes. By definition, $\bar{\omega} = (\omega_{SPP} + \omega_P)/2$. The solution of eqn (4), setting the approximation $F_{SPP} = F_P \sim 0$, leads to the upper $\omega^+$ and lower $\omega^-$ eigen-frequencies (eqn (5)) of the coupled modes.

$$\omega^{+/-} = \bar{\omega} \pm \frac{1}{2}\mathrm{Re}\left[\sqrt{\Omega^2 + \left[\omega_{SPP} - \omega_P + i\left(\frac{\Gamma_{SPP}}{2} - \frac{\Gamma_P}{2}\right)\right]^2}\right] \quad (5)$$

$$C_{ext}(q_{SPP}, \omega) \propto \langle F_P \cdot \dot{x}_P + F_{SPP} \cdot \dot{x}_{SPP} \rangle \quad (6)$$

From that, the coupling strength $\Omega$ is determined by the smallest difference between $\omega^+$ and $\omega^-$. When the strict condition $\eta = 2\Omega/(\Gamma_{SPP} - \Gamma_{PP}) > 1$ is fulfilled,[23,28,46] the interaction is classified in the SC regime. Following the method adopted in ref. 23, we determine the coupling parameters by fitting the extinction coefficient $C_{ext}(q_{SPP},\omega)$ (eqn (6)) to the experimental iso-momentum spectra near the AC region, which correspond to vertical profiles extracted from the experimental dispersion (green and black vertical lines in Fig. 4a). In this approach, it is assumed that the experimental $\mathrm{Re}[\Im(\mathfrak{q},\omega)]$ is proportional to the dissipated power of the coupled system: $\mathrm{Re}[\Im(\mathfrak{q},\omega)] \propto C_{ext}(q_{SPP},\omega)$. Fig. 4c presents iso-momenta data for $q_{SPP}$ = 1.3 × $10^4$ $cm^{-1}$ and $q_{SPP}$ = 1.5 × $10^4$ $cm^{-1}$ and the corresponding fittings from $C_{ext}$ ($q_{SPP},\omega$) (eqn (6)). Using the obtained fitting parameters ($\Omega$ = 41 $cm^{-1}$, $\Gamma_{SPP}$ = 71 $cm^{-1}$ and $\Gamma_{PP}$ = 6 $cm^{-1}$) we compute the $\omega^+$ and $\omega^-$ dispersion branches, which are displayed as red circles in Fig. 4d. This analysis shows that the SC criterion is fulfilled for the SPP–phonon interaction: $\eta = 2\Omega/(\Gamma_{SPP} - \Gamma_{PP})$ = 1.26 satisfying the condition $\eta$ > 1. Thereby, the interaction between SPP waves on Au and in-plane $\omega_{TO}$ phonon of the hexagonal boron nitride (hBN) occurs within the SC regime.

In summary, here we fully characterize the nanophotonic properties of mid-IR SPP waves at the interface formed between hBN 2D crystal and Au surface using s-SNOM and SINS nanoscopies. In the hBN upper RS polaritonic band, we see the interference between SPP waves on the metal layer and HPhP waves in the 2D crystal, creating an SPP–HPhP wave superposition. In contrast to graphene–hyperbolic crystal systems,[44,47,48] where momentum matching forms hybrid waves of one component, SPP–HPhP superposition in hBN/Au arises from interference between polaritons with distinct momenta scales ($q_{SPP} \sim 10^4$ $cm^{-1}$ and $q_{HPhP} \sim 10^5$ $cm^{-1}$), generating a wave with two clearly discernible components.[42,45,46] This effect can be useful for inducing spatial frequency modulation in 2D polariton waves as observed from the fact that the HPhP constitutes a high spatial frequency modulation onto the SPP wave. We also display and quantitatively evaluate the SC regime of the interaction between mid-IR SPP waves with the hBN in-plane $\omega_{TO}$ phonon. Provided the large spectral coverage of SPPs in the IR molecular fingerprint, this ability of the SPP waves to couple with phonons can be exploited for enhanced sensing of other systems including organic and biological materials. Moreover, our study paves the way to future research on the SPP wave properties in interfaces with other 2D materials,[47] with phonon and polaritonic activities in the mid-infrared to the terahertz (THz), including anisotropic hyperbolic crystals[49–54] that might influence the SPP's directionality.

## Experimental Methods

### Scattering-type scanning near-field optical microscopy (s-SNOM)

The s-SNOM (neaSNOM from Neaspec, attocube systems AG) uses a metallic tip of an atomic force microscope (AFM) as an

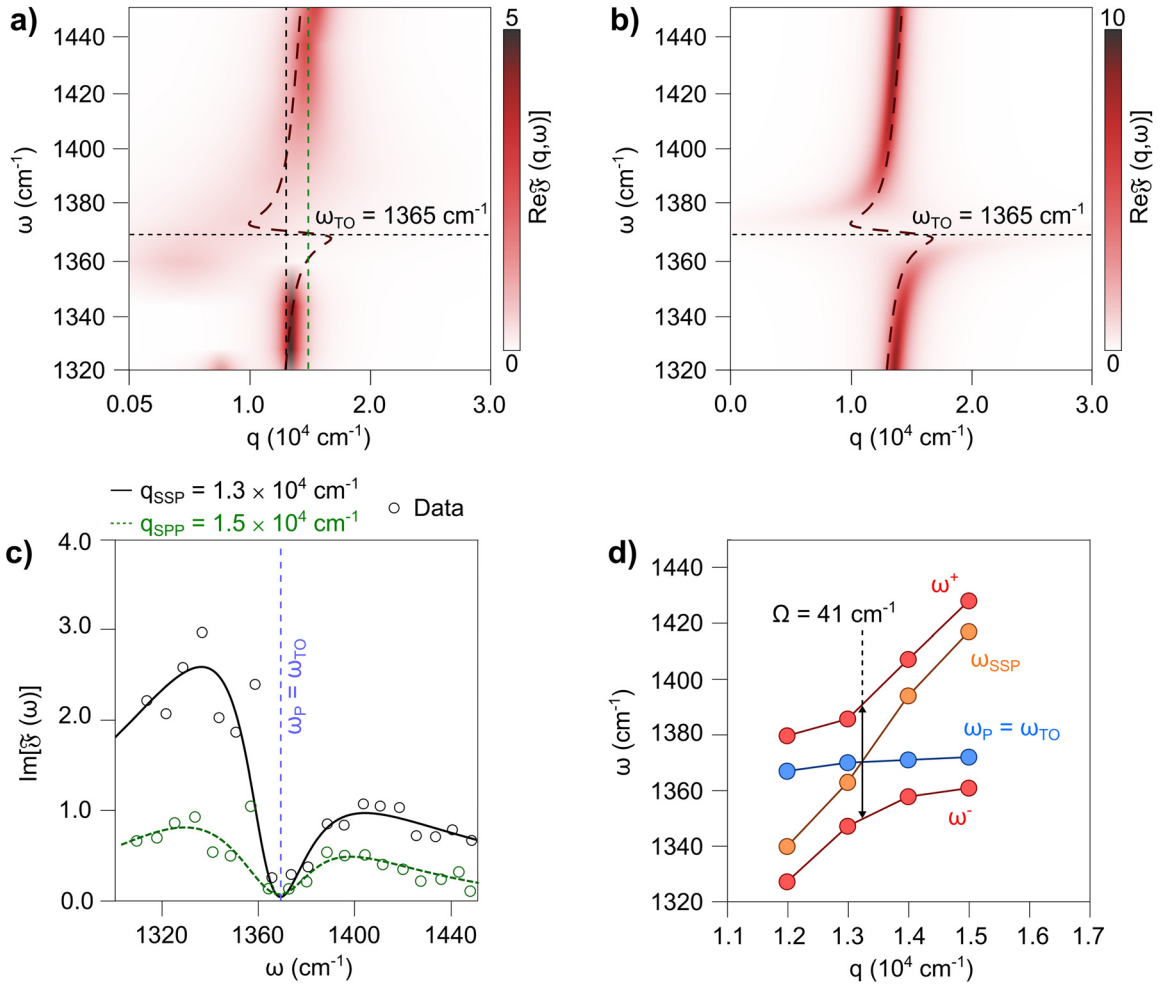


**Fig. 4** SC regime experimental (a) and theoretical (b) dispersion of SPP modes showing the anti-crossing (AC) near $\omega_{TO}$. (c) Isomomentum curves generated from Re$[\Im(q,\omega)]$ and fitting performed by $C_{ext}(q_{SPP},\omega)$. The black curve represents the fit for $q_{SPP}$ = 1.3 × $10^4$ $cm^{-1}$ and the green curve for $q_{SPP}$ = 1.5 × $10^4$ $cm^{-1}$. (d) Dispersion of hybrid modes ($\omega^+/\omega^-$) resulting from the coupling between SPP ($\omega_{SPP}$) and the optical phonon $\omega_P = \omega_{TO}$.

optical nanoprobe to measure the optical near-field. The AFM operates in semi-contact mode wherein a metallic tip, with a 25 nm-large apex radius, is electronically driven to vibrate at its natural mechanical frequency ($\Omega$). The IR illumination is focused on the tip–sample region by a parabolic mirror. As a result, a highly confined optical field rises at the tip apex and causes a local effective polarizability to the tip–sample system due to the lightning rod effect.[55–57] The back-scattered light ($S$) from the tip–sample interaction is collected by the same parabolic mirror and directed to a mercury-cadmium-telluride (MCT) detector. This scattered signal is composed of a mixture of the optical near-field scattering, originating from the local effective polarizability, and high-intensity far-field component (background). To suppress the background, $S$ is demodulated in harmonics ($n$) of $\Omega$, by a lock-in based electronic scheme, and it is used for pseudo-heterodyne (PS-het) detection.[58] Authentic optical near-field measurements are given by high harmonic signals, $n \geq 2$, in combination with PS-het detection. Quantum cascade lasers (QCL) were employed as the illumination sources. Due to the high near-field intensity confined at the tip apex, it becomes an optical nanoprobe of high spatial resolution, approximately equal to the radius, and high momenta capable of exciting HPhP modes.

### Synchrotron infrared nanospectroscopy (SINS)

SINS operates based on s-SNOM principles, particularly, regarding optical near-field excitation and the use of a similar detection scheme. In SINS, an s-SNOM microscope is combined with highly brilliant broadband IR radiation emitted by a synchrotron as the illumination source. The scattered light ($S$) is then directed into an asymmetric Michelson interferometer (Fig. 1a), where it interferes with the reference arm's beam. Analogous to s-SNOM, lock-in detection electronics captures the optical near-field interferograms from the higher harmonics of $S$ ($n \geq 2$). Through Fourier transform, the mid-infrared near-field spectrum is obtained. In this study, SINS experiments were conducted at the Imbuia beamline of Sirius, the Brazilian Synchrotron Light Laboratory (LNLS),[21] using an

 

MCT detector to measure the optical near-field in the range of 650 to 3000 $cm^{-1}$.

### Sample construction

The groove was created by standard photolithography onto $SiO_2$ (2 μm thick)/Si substrates followed by deposition of a 90 nm thick Au film by the electron beam. The hBN flakes were then transferred onto the Au groove using a PDMS-assisted technique.[26] Before hBN transfer, the flakes were exfoliated by the standard scotch tape method on the PDMS stamp and were selected based on optical contrast. After the hBN transfer, the Au disk-like antenna, with an average height of 150 nm and an elliptical basis measuring ~2.4 and ~3.9 μm for the short and long axes respectively, was designed atop the transferred hBN and at the edge of the groove by a new photolithography step, followed by the deposition of a 90 nm thick Au film by electron beam and lift-off.

## Data availability

All data that support the findings of this study are included within the article and its ESI.†

## Conflicts of interest

"The authors declare the following financial interests/personal relationships, which may be considered potential competing interests: Adrian Cernescu is employed by attocube systems AG, a company that manufactures s-SNOM and nano-FTIR spectroscopy instruments".

## Acknowledgements

All Brazilian authors thank the Brazilian Synchrotron Light Source (LNLS) for providing beamtime for SINS and s-SNOM experiments at the Imbuia Beamline of Sirius (Proposal 20232881). NeaSpec GmbH is acknowledged for its technical assistance. F. H. F. and R. O. F. acknowledge FAPESP support through the postdoc grant 2023/09839-5. F. C. B. M., and I. D. B. acknowledge financial support from the FAPESP (2022/02901-4). I. D. B., R. O. F. and F. C. B. M. acknowledge the CNPq through research grants 311327/2020-6, 311564/2018-6, and 306170/2023-0, respectively. R. O. F. acknowledges the support from the FAPESP Young Investigator grant 2019/14017-9. I. D. B. acknowledges the financial support from the Brazilian Nanocarbon Institute of Science and Technology (INCT/Nanocarbono). D. A. B. acknowledges support from CAPES-PRINT (88887.310281/2018-00) and Mackpesquisa. The authors also thank the Brazilian Nanotechnology National Laboratory (LNNano) and LNLS, both part of the Brazilian Centre for Research in Energy and Materials (CNPEM), a private non-profit organization under the supervision of the Brazilian Ministry for Science, Technology, and Innovations (MCTI), for sample preparation and characterization.

## References

1 S. A. Maier, *Plasmonics: Fundamentals and Applications*, Springer US, New York, NY, 2007.
2 Z. Han and S. I. Bozhevolnyi, Radiation guiding with surface plasmon polaritons, *Rep. Prog. Phys.*, 2013, **76**(1), 016402.
3 V. G. Achanta, Surface waves at metal-dielectric interfaces: Material science perspective, *Rev. Phys*, 2020, **5**, 100041.
4 Y. Fang and M. Sun, Nanoplasmonic waveguides: towards applications in integrated nanophotonic circuits, *Light:Sci. Appl.*, 2015, **4**(6), e294–e294.
5 H. Yu, Y. Peng, Y. Yang and Z.-Y. Li, Plasmon-enhanced light–matter interactions and applications, *npj Comput. Mater.*, 2019, **5**(1), 45.
6 Y. J. Lu, J. Kim, H. Y. Chen, C. Wu, N. Dabidian, C. E. Sanders, C. Y. Wang, M. Y. Lu, B. H. Li, X. Qiu, W. H. Chang, L. J. Chen, G. Shvets, C. K. Shih and S. Gwo, Plasmonic nanolaser using epitaxially grown silver film, *Science*, 2012, **337**(6093), 450–453.
7 R. Chandrasekar, Z. Wang, X. Meng, S. I. Azzam, M. Y. Shalaginov, A. Lagutchev, Y. L. Kim, A. Wei, A. V. Kildishev, A. Boltasseva and V. M. Shalaev, Lasing Action with Gold Nanorod Hyperbolic Metamaterials, *ACS Photonics*, 2017, **4**(3), 674–680.
8 D. J. Bergman and M. I. Stockman, Surface Plasmon Amplification by Stimulated Emission of Radiation: Quantum Generation of Coherent Surface Plasmons in Nanosystems, *Phys. Rev. Lett.*, 2003, **90**(2), 027402.
9 T. J. Davis, D. E. Gómez and A. Roberts, Plasmonic circuits for manipulating optical information, *Nanophotonics*, 2016, **6**(3), 543–559.
10 M. Schnell, P. Alonso-González, L. Arzubiaga, F. Casanova, L. E. Hueso, A. Chuvilin and R. Hillenbrand, Nanofocusing of mid-infrared energy with tapered transmission lines, *Nat. Photonics*, 2011, **5**(5), 283–287.
11 P. Sarriugarte, M. Schnell, P. Alonso-González, L. Arzubiaga, F. Golmar, F. Casanova, L. E. Hueso and R. Hillenbrand, Propagation and nanofocusing of infrared surface plasmons on tapered transmission lines: Influence of the substrate, *Opt. Commun.*, 2012, **285**(16), 3378–3382.
12 P. Sarriugarte, M. Schnell, A. Chuvilin and R. Hillenbrand, Polarization-Resolved Near-Field Characterization of Nanoscale Infrared Modes in Transmission Lines Fabricated by Gallium and Helium Ion Beam Milling, *ACS Photonics*, 2014, **1**(7), 604–611.
13 P. Pons-Valencia, F. J. Alfaro-Mozaz, M. M. Wiecha, V. Biolek, I. Dolado, S. Vélez, P. Li, P. Alonso-González, F. Casanova, L. E. Hueso, L. Martín-Moreno, R. Hillenbrand and A. Y. Nikitin, Launching of hyperbolic phonon-polaritons in h-BN slabs by resonant metal plasmonic antennas, *Nat. Commun.*, 2019, **10**(1), 3242.
14 Y. Zhang, C. Hu, B. Lyu, H. Li, Z. Ying, L. Wang, A. Deng, X. Luo, Q. Gao, J. Chen, J. Du, P. Shen, K. Watanabe, T. Taniguchi, J.-H. Kang, F. Wang, Y. Zhang and Z. Shi, Tunable Cherenkov Radiation of Phonon Polaritons in

Silver Nanowire/Hexagonal Boron Nitride Heterostructures, *Nano Lett.*, 2020, **20**(4), 2770–2777.
15 X. Chen, X. Liu, X. Guo, S. Chen, H. Hu, E. Nikulina, X. Ye, Z. Yao, H. A. Bechtel, M. C. Martin, G. L. Carr, Q. Dai, S. Zhuang, Q. Hu, Y. Zhu, R. Hillenbrand, M. Liu and G. You, THz Near-Field Imaging of Extreme Subwavelength Metal Structures, *ACS Photonics*, 2020, **7**(3), 687–694.
16 K. Aleshire, I. M. Pavlovetc, R. Collette, X.-T. Kong, P. D. Rack, S. Zhang, D. J. Masiello, J. P. Camden, G. V. Hartland and M. Kuno, Far-field midinfrared superresolution imaging and spectroscopy of single high aspect ratio gold nanowires, *Proc. Natl. Acad. Sci. U. S. A.*, 2020, **117**(5), 2288–2293.
17 R. Stanley, Plasmonics in the mid-infrared, *Nat. Photonics*, 2012, **6**(7), 409–411.
18 T. Taliercio and P. Biagioni, Semiconductor infrared plasmonics, *Nanophotonics*, 2019, **8**(6), 949–990.
19 Y. Zhong, S. D. Malagari, T. Hamilton and D. Wasserman, Review of mid-infrared plasmonic materials, *J. Nanophotonics*, 2015, **9**(1), 093791.
20 X. Chen, D. Hu, R. Mescall, G. You, D. N. Basov, Q. Dai and M. Liu, Modern Scattering-Type Scanning Near-Field Optical Microscopy for Advanced Material Research, *Adv. Mater.*, 2019, **31**(24), 1804774.
21 R. A. Mayer, F. H. Feres and R. O. Freitas, Synchrotron infrared nanospectroscopy as a game changer in nanophotonics, in *2021 SBFoton International Optics and Photonics Conference (SBFoton IOPC)*, IEEE, 2021, pp. 1–6.
22 D. S. Dovzhenko, S. V. Ryabchuk, Y. P. Rakovich and I. R. Nabiev, Light–matter interaction in the strong coupling regime: configurations, conditions, and applications, *Nanoscale*, 2018, **10**(8), 3589–3605.
23 A. Bylinkin, M. Schnell, M. Autore, F. Calavalle, P. Li, J. Taboada-Gutièrrez, S. Liu, J. H. Edgar, F. Casanova, L. E. Hueso, P. Alonso-Gonzalez, A. Y. Nikitin and R. Hillenbrand, Real-space observation of vibrational strong coupling between propagating phonon polaritons and organic molecules, *Nat. Photonics*, 2021, **15**(3), 197–202.
24 A. J. Sternbach, S. L. Moore, A. Rikhter, S. Zhang, R. Jing, Y. Shao, B. S. Y. Kim, S. Xu, S. Liu, J. H. Edgar, A. Rubio, C. Dean, J. Hone, M. M. Fogler and D. N. Basov, Negative refraction in hyperbolic hetero-bicrystals, *Science*, 2023, **379**(6632), 555–557.
25 L. Wehmeier, S. Yu, X. Chen, R. A. Mayer, L. Xiong, H. Yao, Y. Jiang, J. Hu, E. Janzen, J. H. Edgar, X. Zheng, T. F. Heinz, D. N. Basov, C. C. Homes, G. Hu, G. L. Carr, M. Liu and J. A. Fan, Tunable Phonon Polariton Hybridization in a van der Waals Hetero-Bicrystal, *Adv. Mater.*, 2024, **36**(33), 2401349.
26 I. D. Barcelos, A. R. Cadore, L. C. Campos, A. Malachias, K. Watanabe, T. Taniguchi, F. C. B. Maia, R. Freitas and C. Deneke, Graphene/h-BN plasmon–phonon coupling and plasmon delocalization observed by infrared nano-spectroscopy, *Nanoscale*, 2015, **7**(27), 11620–11625.
27 I. J. Luxmoore, C. H. Gan, P. Q. Liu, F. Valmorra, P. Li, J. Faist and G. R. Nash, Strong Coupling in the Far-Infrared between Graphene Plasmons and the Surface Optical Phonons of Silicon Dioxide, *ACS Photonics*, 2014, **1**(11), 1151–1155.
28 G. Németh, K. Otsuka, D. Datz, Á. Pekker, S. Maruyama, F. Borondics and K. Kamarás, Direct Visualization of Ultrastrong Coupling between Luttinger-Liquid Plasmons and Phonon Polaritons, *Nano Lett.*, 2022, **22**(8), 3495–3502.
29 S. Dai, J. Quan, G. Hu, C.-W. Qiu, T. H. Tao, X. Li and A. Alù, Hyperbolic Phonon Polaritons in Suspended Hexagonal Boron Nitride, *Nano Lett.*, 2019, **19**(2), 1009–1014.
30 F. H. Feres, R. A. Mayer, I. D. Barcelos, R. O. Freitas and F. C. B. Maia, Acceleration of Subwavelength Polaritons by Engineering Dielectric-Metallic Substrates, *ACS Photonics*, 2020, **7**(6), 1396–1402.
31 S. Dai, Q. Ma, T. Andersen, A. S. Mcleod, Z. Fei, M. K. Liu, M. Wagner, K. Watanabe, T. Taniguchi, M. Thiemens, F. Keilmann, P. Jarillo-Herrero, M. M. Fogler and D. N. Basov, Subdiffractional focusing and guiding of polaritonic rays in a natural hyperbolic material, *Nat. Commun.*, 2015, **6**(1), 6963.
32 S. Dai, Z. Fei, Q. Ma, A. S. Rodin, M. Wagner, A. S. McLeod, M. K. Liu, W. Gannett, W. Regan, K. Watanabe, T. Taniguchi, M. Thiemens, G. Dominguez, A. H. C. Neto, A. Zettl, F. Keilmann, P. Jarillo-Herrero, M. M. Fogler and D. N. Basov, Tunable Phonon Polaritons in Atomically Thin van der Waals Crystals of Boron Nitride, *Science*, 2014, **343**(6175), 1125–1129.
33 J. Duan, R. Chen, J. Li, K. Jin, Z. Sun and J. Chen, Launching Phonon Polaritons by Natural Boron Nitride Wrinkles with Modifiable Dispersion by Dielectric Environments, *Adv. Mater.*, 2017, **29**(38), 1702494.
34 F. H. Feres, I. D. Barcelos, R. A. Mayer, T. M. dos Santos, R. O. Freitas, M. B. Raschke, D. A. Bahamon and F. C. B. Maia, Dipole modelling for a robust description of subdiffractional polariton waves, *Nanoscale*, 2019, **11**(44), 21218–21226.
35 S. G. Menabde, J. T. Heiden, J. D. Cox, N. A. Mortensen and M. S. Jang, Image polaritons in van der Waals crystals, *Nanophotonics*, 2022, **11**(11), 2433–2452.
36 S. G. Menabde, S. Boroviks, J. Ahn, J. T. Heiden, K. Watanabe, T. Taniguchi, T. Low, D. K. Hwang, N. A. Mortensen and M. S. Jang, Near-field probing of image phonon-polaritons in hexagonal boron nitride on gold crystals, *Sci. Adv.*, 2022, **8**(28), eabn0627.
37 J. Jacob, A. Babu, G. Mathew and V. Mathew, Propagation of surface plasmon polaritons in anisotropic MIM and IMI structures, *Superlattices Microstruct.*, 2008, **44**(3), 282–290.
38 A. Mancini, L. Nan, F. J. Wendisch, R. Berté, H. Ren, E. Cortés and S. A. Maier, Near-Field Retrieval of the Surface Phonon Polariton Dispersion in Free-Standing Silicon Carbide Thin Films, *ACS Photonics*, 2022, **9**(11), 3696–3704.
39 F. Walla, M. M. Wiecha, N. Mecklenbeck, S. Beldi, F. Keilmann, M. D. Thomson and H. G. Roskos, Anisotropic excitation of surface plasmon polaritons on a

 

metal film by a scattering-type scanning near-field microscope with a non-rotationally-symmetric probe tip, *Nanophotonics*, 2018, **7**(1), 269–276.

40 A. Ambrosio, M. Tamagnone, K. Chaudhary, L. A. Jauregui, P. Kim, W. L. Wilson and F. Capasso, Selective excitation and imaging of ultraslow phonon polaritons in thin hexagonal boron nitride crystals, *Light:Sci. Appl.*, 2018, **7**(1), 27.

41 A. Andryieuski, V. A. Zenin, R. Malureanu, V. S. Volkov, S. I. Bozhevolnyi and A. V. Lavrinenko, Direct Characterization of Plasmonic Slot Waveguides and Nanocouplers, *Nano Lett.*, 2014, **14**(7), 3925–3929.

42 F. C. B. Maia, B. T. O'Callahan, A. R. Cadore, I. D. Barcelos, L. C. Campos, K. Watanabe, T. Taniguchi, C. Deneke, A. Belyanin, M. B. Raschke and R. O. Freitas, Anisotropic Flow Control and Gate Modulation of Hybrid Phonon-Polaritons, *Nano Lett.*, 2019, **19**(2), 708–715.

43 I. D. Barcelos, H. A. Bechtel, C. J. S. de Matos, D. A. Bahamon, B. Kaestner, F. C. B. Maia and R. O. Freitas, Probing Polaritons in 2D Materials with Synchrotron Infrared Nanospectroscopy, *Adv. Opt. Mater.*, 2020, **8**(5), 1901091.

44 M. Autore, P. Li, I. Dolado, F. J. Alfaro-Mozaz, R. Esteban, A. Atxabal, F. Casanova, L. E. Hueso, P. Alonso-González, J. Aizpurua, A. Y. Nikitin, S. Vélez and R. Hillenbrand, Boron nitride nanoresonators for phonon-enhanced molecular vibrational spectroscopy at the strong coupling limit, *Light:Sci. Appl.*, 2017, **7**(4), 17172–17172.

45 S. Dai, Q. Ma, M. K. Liu, T. Andersen, Z. Fei, M. D. Goldflam, M. Wagner, K. Watanabe, T. Taniguchi, M. Thiemens, F. Keilmann, G. C. A. M. Janssen, S.-E. Zhu, P. Jarillo-Herrero, M. M. Fogler and D. N. Basov, Graphene on hexagonal boron nitride as a tunable hyperbolic metamaterial, *Nat. Nanotechnol.*, 2015, **10**(8), 682–686.

46 Y. Zeng, Q. Ou, L. Liu, C. Zheng, Z. Wang, Y. Gong, X. Liang, Y. Zhang, G. Hu, Z. Yang, C.-W. Qiu, Q. Bao, H. Chen and Z. Dai, Tailoring Topological Transitions of Anisotropic Polaritons by Interface Engineering in Biaxial Crystals, *Nano Lett.*, 2022, **22**(10), 4260–4268.

47 I. D. Barcelos, A. R. Cadore, A. B. Alencar, F. C. B. Maia, E. Mania, R. F. Oliveira, C. C. B. Bufon, Â. Malachias, R. O. Freitas, R. L. Moreira and H. Chacham, Infrared Fingerprints of Natural 2D Talc and Plasmon–Phonon Coupling in Graphene–Talc Heterostructures, *ACS Photonics*, 2018, **5**(5), 1912–1918.

48 W. Ma, P. Alonso-González, S. Li, A. Y. Nikitin, J. Yuan, J. Martín-Sánchez, J. Taboada-Gutiérrez, I. Amenabar, P. Li, S. Vélez, C. Tollan, Z. Dai, Y. Zhang, S. Sriram, K. Kalantar-Zadeh, S.-T. Lee, R. Hillenbrand and Q. Bao, In-plane anisotropic and ultra-low-loss polaritons in a natural van der Waals crystal, *Nature*, 2018, **562**(7728), 557–562.

49 F. H. Feres, R. A. Mayer, L. Wehmeier, F. C. B. Maia, E. R. Viana, A. Malachias, H. A. Bechtel, J. M. Klopf, L. M. Eng, S. C. Kehr, J. C. González, R. O. Freitas and I. D. Barcelos, Sub-diffractional cavity modes of terahertz hyperbolic phonon polaritons in tin oxide, *Nat. Commun.*, 2021, **12**(1), 1995.

50 J. Taboada-Gutiérrez, G. Álvarez-Pérez, J. Duan, W. Ma, K. Crowley, I. Prieto, A. Bylinkin, M. Autore, H. Volkova, K. Kimura, T. Kimura, M.-H. Berger, S. Li, Q. Bao, X. P. A. Gao, I. Errea, A. Y. Nikitin, R. Hillenbrand, J. Martín-Sánchez and P. Alonso-González, Broad spectral tuning of ultra-low-loss polaritons in a van der Waals crystal by intercalation, *Nat. Mater.*, 2020, **19**(9), 964–968.

51 R. A. Mayer, L. Wehmeier, M. Torquato, X. Chen, F. H. Feres, F. C. B. Maia, M. Obst, F. G. Kaps, A. Luferau, J. M. Klopf, S. N. Gilbert Corder, H. A. Bechtel, J. C. González, E. R. Viana, L. M. Eng, S. C. Kehr, R. O. Freitas and I. D. Barcelos, Paratellurite Nanowires as a Versatile Material for THz Phonon Polaritons, *ACS Photonics*, 2024, 4323–4333.

52 S.-J. Yu, H. Yao, G. Hu, Y. Jiang, X. Zheng, S. Fan, T. F. Heinz and J. A. Fan, Hyperbolic Polaritonic Rulers Based on van der Waals α-$MoO_3$ Waveguides and Resonators, *ACS Nano*, 2023, **17**(22), 23057–23064.

53 F. Keilmann and R. Hillenbrand, Near-field microscopy by elastic light scattering from a tip, *Philos. Trans. R. Soc., A*, 2004, **362**(1817), 787–805.

54 F. G. Kaps, S. C. Kehr and L. M. Eng, Polarization Sensitivity in Scattering-Type Scanning Near-Field Optical Microscopy—Towards Nanoellipsometry, *Appl. Sci.*, 2023, **13**(18), 10429.

55 R. Hillenbrand and F. Keilmann, Complex Optical Constants on a Subwavelength Scale, *Phys. Rev. Lett.*, 2000, **85**(14), 3029–3032.

56 N. Ocelic, A. Huber and R. Hillenbrand, Pseudoheterodyne detection for background-free near-field spectroscopy, *Appl. Phys. Lett.*, 2006, **89**(10), 101124.

57 T. M. Santos, S. Lordano, R. A. Mayer, L. Volpe, G. M. Rodrigues, B. Meyer, H. Westfahl Jr and R. O. Freitas, Synchrotron infrared nanospectroscopy in fourth-generation storage rings, *J. Synchrotron Radiat.*, 2024, **31**(3), 547–556.

58 R. Cunha, A. Cadore, S. L. L. M. Ramos, K. Watanabe, T. Taniguchi, S. Kim, A. S. Solntsev, I. Aharonovich and L. M. Malard, Second harmonic generation in defective hexagonal boron nitride, *J. Phys.: Condens. Matter*, 2020, **32**(19), 19LT01.